Book of Tutorials and Abstracts

European Microbeam Analysis Society

EMAS 2026

15th

REGIONAL WORKSHOP

TOPICAL CONFERENCE ON ELECTRON BACKSCATTER DIFFRACTION (EBSD)

14 to 17 June 2026
at the
CentraleSupélec, Gif-sur-Yvette, France

Organised in collaboration with:
ICMMO, ENS Paris-Saclay,
Université Paris-Saclay

EMAS
European Microbeam Analysis Society eV
www.microbeamanalysis.eu/

This volume is published by:
European Microbeam Analysis Society eV (EMAS)
EMAS Secretariat
c/o Eidgenössische Technische Hochschule, Department of Earth and Planetary Sciences
Clausiusstrasse 25
8092 Zürich
Switzerland

ISBN 978 90 8227 6992
NUR code: 971 – Materials Science

THE INCREASING MULTI-FUNCTIONALITY OF HIGH-RESOLUTION EBSD

Qiwei Shi[1,*], D. Loisnard[2], M. Mollens[2] and S. Roux[3]

1 SJTU-Paris Elite Institute of Technology, Shanghai Jiao Tong University
200240 Shanghai, P.R. China
2 EdF R&D, Site des Renardières
avenue des Renardières, Ecuelles, 77818 Moret-sur-Loing, France
3 Université Paris-Saclay, CentraleSupélec, ENS Paris-Saclay, CNRS, LMPS - Laboratoire de Mécanique Paris-Saclay
91190, Gif-sur-Yvette, France
e-mail: sqw@sjtu.edu.cn

Qiwei Shi, teaching-research-track associate professor at Shanghai Jiao Tong University, P.R. China. He earned a PhD degree from ENS Paris-Saclay in 2018 under the supervision of François Hild and Stéphane Roux. His major research interests lie in digital image correlation (DIC), high-resolution electron backscatter diffraction (HR-EBSD) developments and application, and crystal plasticity simulation. He has more than 40 publications in SCI journals including Ultramicroscopy, Mater. Charact, Meas. Sci. Technol., Micron, Nat. Mater., Int. J. Plast, Acta Mater., and JMPS. He has received two grants of the National Natural Science Foundation of China, industrial grants from Tescan Microscopy and EDF. He has also published two textbooks on fluid dynamics and electric circuits in P.R. China.

1. ABSTRACT

The advent of advanced correlation-based high-resolution electron backscatter diffraction (HR-EBSD) techniques offers the opportunity to retrieve more and more of the rich information contained in the diffraction patterns. During the last two decades, HR-EBSD has evolved into a multi-functional characterisation technique. Relative and absolute stress components, geometrically necessary and statistically stored dislocations, surface topography, lattice constant parameters, imperfections of EBSD system such as the pattern distortion, temperature, …, the list of physical quantities is ever growing. Besides, characterisation evolves from qualitative to quantitative, and from low to high precision. The increasing multi-functionality of HR-EBSD broadens the horizon for numerous applications, especially in materials science, micromechanics and for the semiconductor industry.

2. INTRODUCTION

The HR-EBSD technique has drawn attention in the last two decades, mainly thanks to its ability to assess the elastic strain/stress state with a sub-micron spatial resolution. However, the complex interaction between the incident electron beam and the sample offers the possibility to access other physical quantities, including the dislocation density, surface roughness and even temperature. This talk will list and discuss these various characterisation focusses of HR-EBSD within a unified framework.

3. RELATIVE ELASTIC STRAIN/STRESS

The first and most important parameter targeted by HR-EBSD is the elastic strain. Cross-correlation-based digital image correlation is used to register reference and current EBSPs, with a non-rigid transformation which encodes 8 out of 9 components of the elastic displacement gradient tensor $\boldsymbol{F}_e$ of the observed material surface [1]. The 9th one corresponds to the hydrostatic dilatation and is inaccessible by the correlation itself. It is often completed by the stress equilibrium condition, such as the plane-stress hypothesis [2]. It is of utmost importance to note that the $\boldsymbol{F}_e$ is relative to the reference pattern, thus the elastic strain/stress calculated by $\boldsymbol{F}_e$ is also relative. The choice of reference pattern impacts the resulting strain fields directly. For several cases, strain-free EBSPs are available and they are the ideal reference patterns. Figure 1 lists two examples, i.e., a thin $Si_{1-x}Ge_x$ layer grown epitaxially on Si substrates [3] and a 4-point bending test where a neutral axis exists. For these cases, experimental-reference HR-EBSD evaluates convincingly the elastic strain/stress maps of the sample.

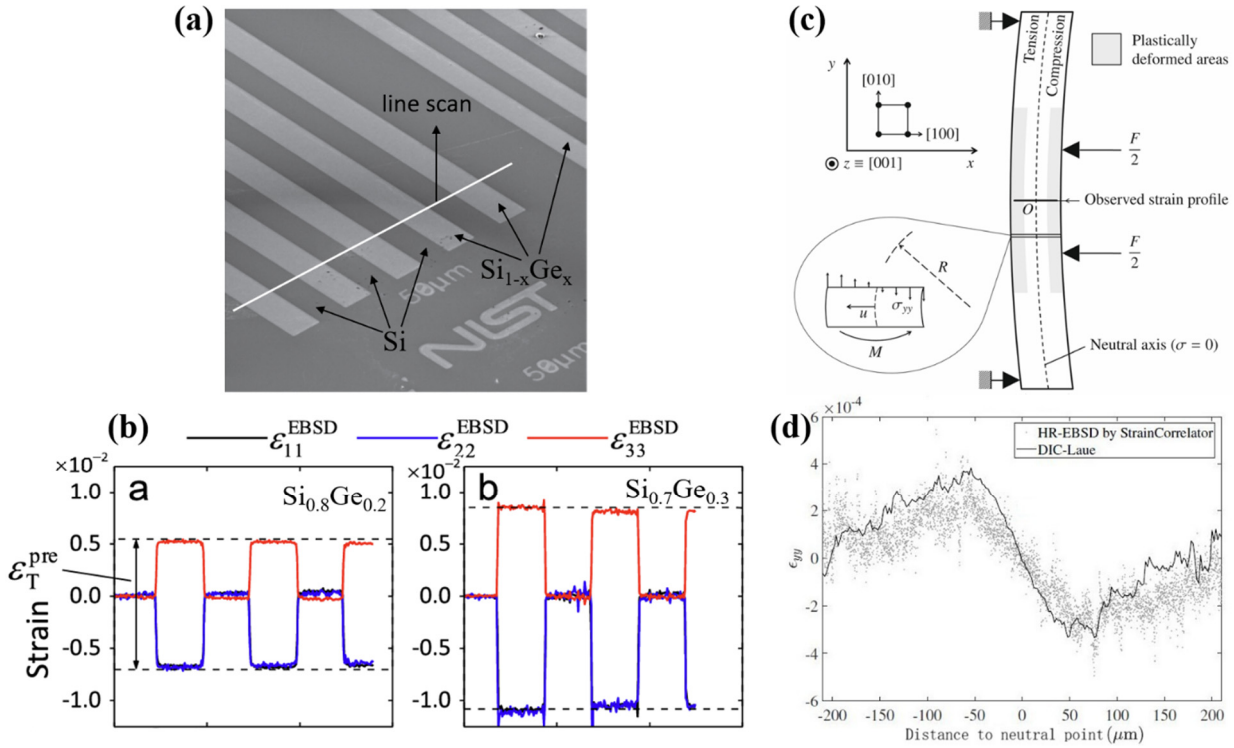

Figure 1. Examples of successful (relative) stress/strain mapping by HR-EBSD. a) EBSD line scan on a standard Si/$Si_{1-x}Ge_x$ sample [3]. b) The strain profiles evaluated by HR-EBSD for Si/$Si_{0.8}Ge_{0.2}$ and Si/$Si_{0.7}Ge_{0.3}$ [3]. c) The experimental setup of a 4-point bending test on asingle crystal 316 stainless steel [4]. d) The ε_{yy} profile estimated by HR-EBSD and DIC-Laue techniques [4].

4. *ABSOLUTE ELASTIC STRAIN/STRESS*

For most cases, there exists no a priori traction-free pixel and it poses a long-lasting problem for the HR-EBSD community. Numerous techniques have been proposed to access the absolute strain/stress values, well summarised by a recent review article [5].

Various groups have attempted to evaluate the absolute residual stress with simulated traction-free reference diffraction patterns. The adopted simulation model, be it dynamical or kinematic, also influences the performance of HR-EBSD. Dynamical simulations lead to a much better similarity with experimental EBSP, thus a better HR-EBSD precision [6]. Alkorta [7] proposed a hybrid HR-EBSD algorithm to retrieve the absolute strain state, i.e., using simultaneously experimental and simulated patterns as reference. Several works tested the performance of using purely simulated reference in retrieving the absolute strain level on virtual datasets [8, 9] or experimental datasets [10, 11].

Attempts have also been made to assess the absolute stress/strain based solely on experimental reference patterns. The stress equilibrium conditions, including the zero divergence in absence

of the body force and the traction-free surface hypothesis, are employed to estimate the strain state of the reference pattern [12]:

$$\sigma^{\mathrm{abs}} = \sigma^{\mathrm{rel}} + \sigma_i^{\mathrm{ref}} \tag{1}$$

where σ_i^{ref} is the stress of the reference pixel of grain i. An example of the stress evaluation is shown in Figure 2. Note that the macroscopic stress level is not accessible by this method.

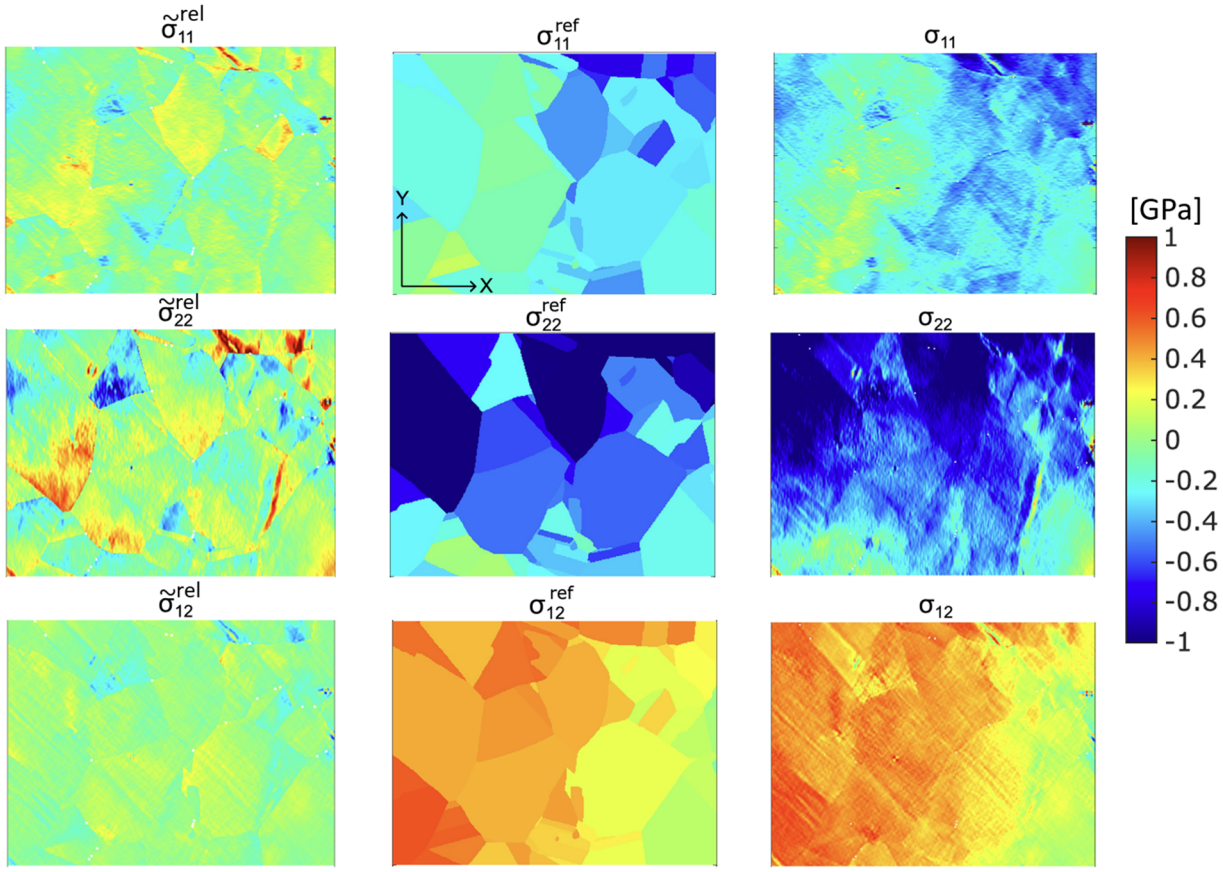

Figure 2. Smoothed relative stress components (left), grain-wise reference stress components (middle) and absolute stress components without the average macroscopic stress (right) for a polycrystal 316L stainless steel sample [12]. The stress states of the reference pixels are estimated by stress equilibrium and traction-free surface hypothesis.

5. GEOMETRICALLY NECESSARY DISLOCATIONS

The GND density can be evaluated theoretically from the crystal lattice curvature, via the famous Nye's tensor. Pantleon [13] proposed a method to resolve the total GND density on each dislocation system thanks to an additional condition, i.e., minimising the strain energy due to dislocations. This strategy has greatly benefitted from the higher angular resolution of HR-EBSD, and helped to characterise GND density map for nickel single crystal [14] and

polycrystal Al-Mg alloys [15]. An example of the GND density map is shown in Fig. 3. The correctness of the GND distribution is cross-validated by TEM observations [15].

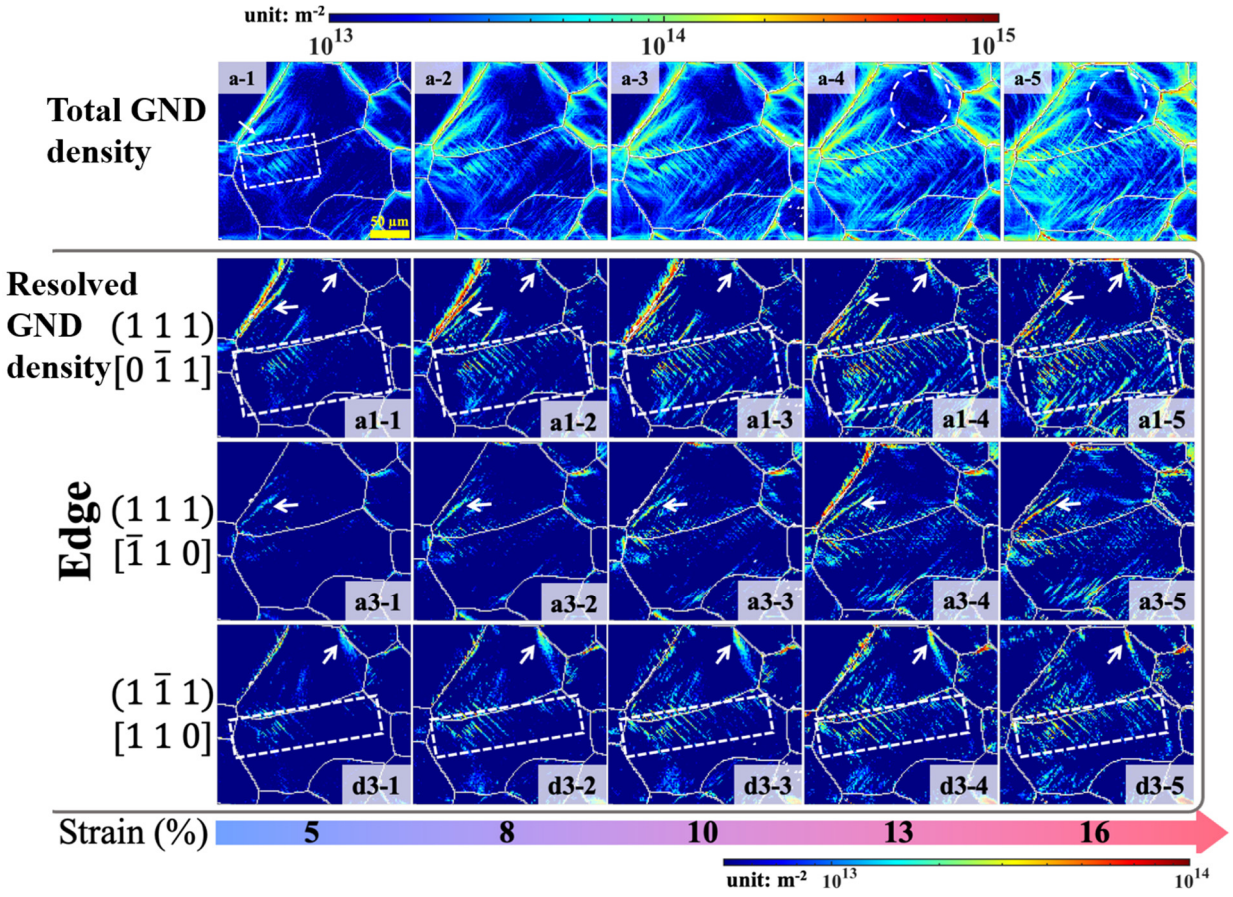

Figure 3. Full field mapping of total GND density and resolved GND density on different slip systems for a polycrystal Al-Mg alloy [15].

6. *OVERALL DISLOCATIONS*

The overall dislocation density, including the GND and statistically stored dislocations, affects the EBSP sharpness. Several metrics have been proposed in the literature. Wang *et al.* [16] uses a pattern sharpness indicator, evaluated in Fourier space, to qualitatively characterise the dislocation densities, as shown in Figs. 4a and 4b. A correlation scheme is proposed by Wu *et al.* [17] to retrieve the smoothness of K-band profiles, providing a semi-quantitatively map of the dislocation densities, see Figs. 4c and 4d.

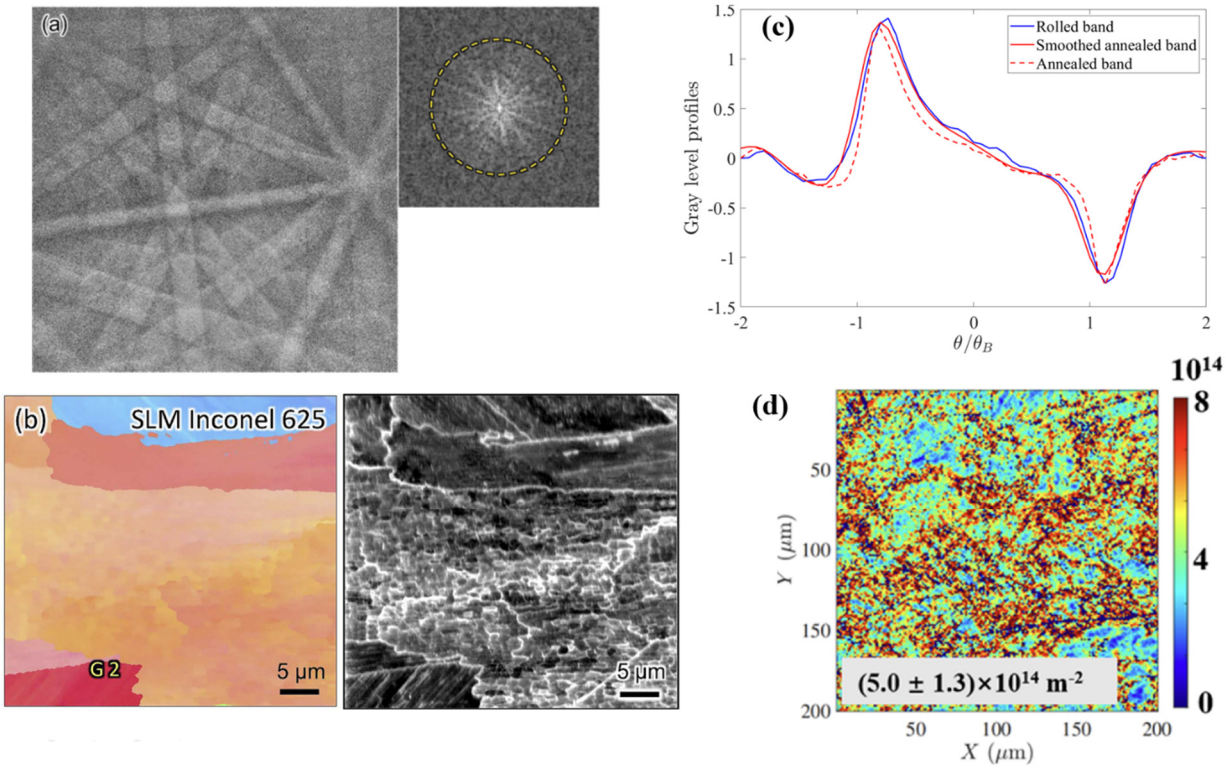

Figure 4. Methods for characterising the dislocation density. a) Pattern sharpness evaluated by the fast Fourier transform. b) The IPF-Z map and EBSP sharpness map of a selected-laser-melted Ni sample, which reflects the elastic strain field from dislocations [16]. c) The K-band brightness profiles of annealed and rolled Al samples, before and after the smoothing operation. d) The total dislocation density mapping of a pure Cu sample by evaluating the K-band profile smoothness [17].

7. *SURFACE ROUGHNESS*

The diffuse backscatter electron (BSE) signal is related to the sample tilt angle. Callahan *et al.* [18] combines the location of the maximum background intensity with Monte Carlo simulations to determine the local surface normals at each point in an EBSD scan. A surface height map is then reconstructed from the local surface normals. Figure 5 shows the topography map, of a Ni sample machined with a femtosecond laser, measured by atomic force microscopy and EBSD patterns. The topography resolution of the technique is evaluated to be around 8 nm.

8. *IMPERFECTIONS (OR ARTEFACTS) OF SEM-EBSD SYSTEM*

The analysis of EBSPs since the beginning of EBSD has been based on an ideal model in terms of projection geometry and pattern brightness distribution. The former assumes that the BSE electrons of homogeneous energy are directly projected onto the screen and loyally imaged, without electromagnetic or optical distortions. The latter proposes that the pixels are brighter inside the Kikuchi bands and darker outside, and the brightness profile across the K-bands is

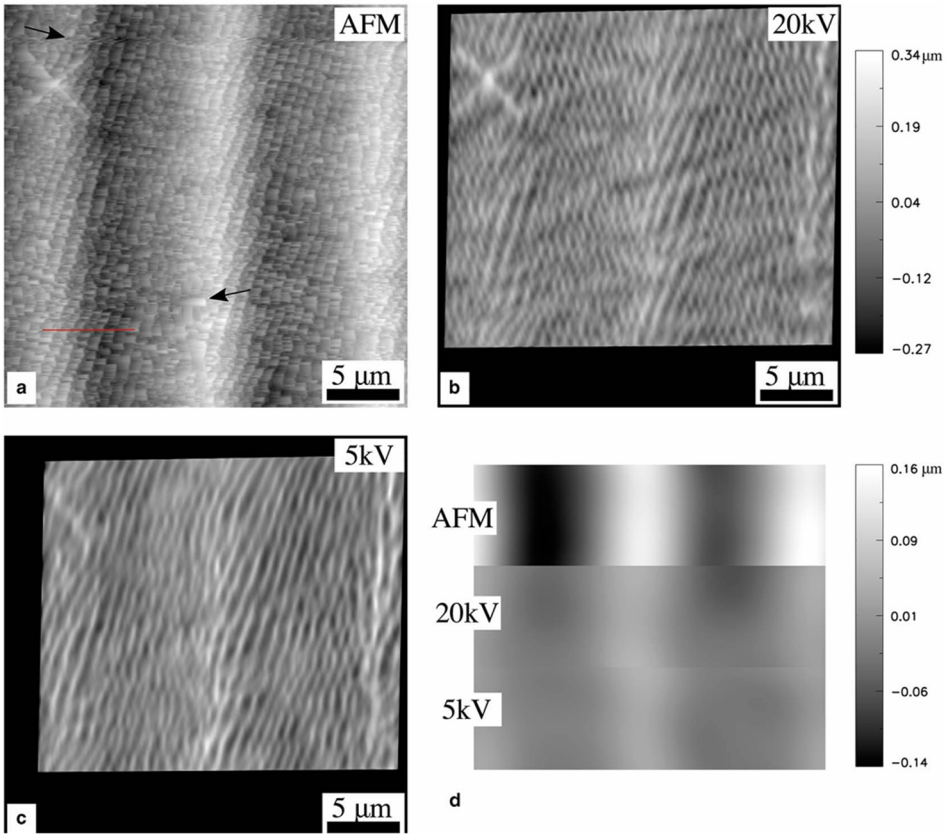

Figure 5. Topography maps from the same region of a laser-machined sample as determined with a) atomic force microscopy (AFM) and with reconstructions from EBSD pattern collected at accelerating voltages of b) 20 kV and c) 5 kV. d) Low frequency information of the surfaces [18].

symmetric. The EBSP simulation methods, including EMSOFT [19] (Bloch wave method), Bohmian trajectory [20] and MS5 [21] (multi-slice method), all adopt these hypotheses. As a result, any deviation from these hypotheses (or any physical effect that is not modelled properly) will lead to systematic errors in simulation-based HR-EBSD techniques. Figure 6 illustrates several imperfections of EBSD data, including the heterogeneous BSE energy distribution, optical distortion, brightness reversal and excess-deficiency effect (more of a specificity of experimental EBSPs).

Efforts have been made to correct or accommodate these imperfections of experimental patterns in their correlation with simulated master patterns, such as calibrating the energy distribution of backscattered electrons (BSE) [22], the radial distortions of EBSPs [23, 24], and mitigating the brightness dissymmetry by gradient operations [25, 26]. Resolving these imperfections improves significantly the HR-EBSD accuracy, especially for the absolute strain results.

End users of EBSD techniques are probably not interested in the artefacts of SEM-EBSD systems listed above, but EBSD developers and microscopists need to be well aware of them.

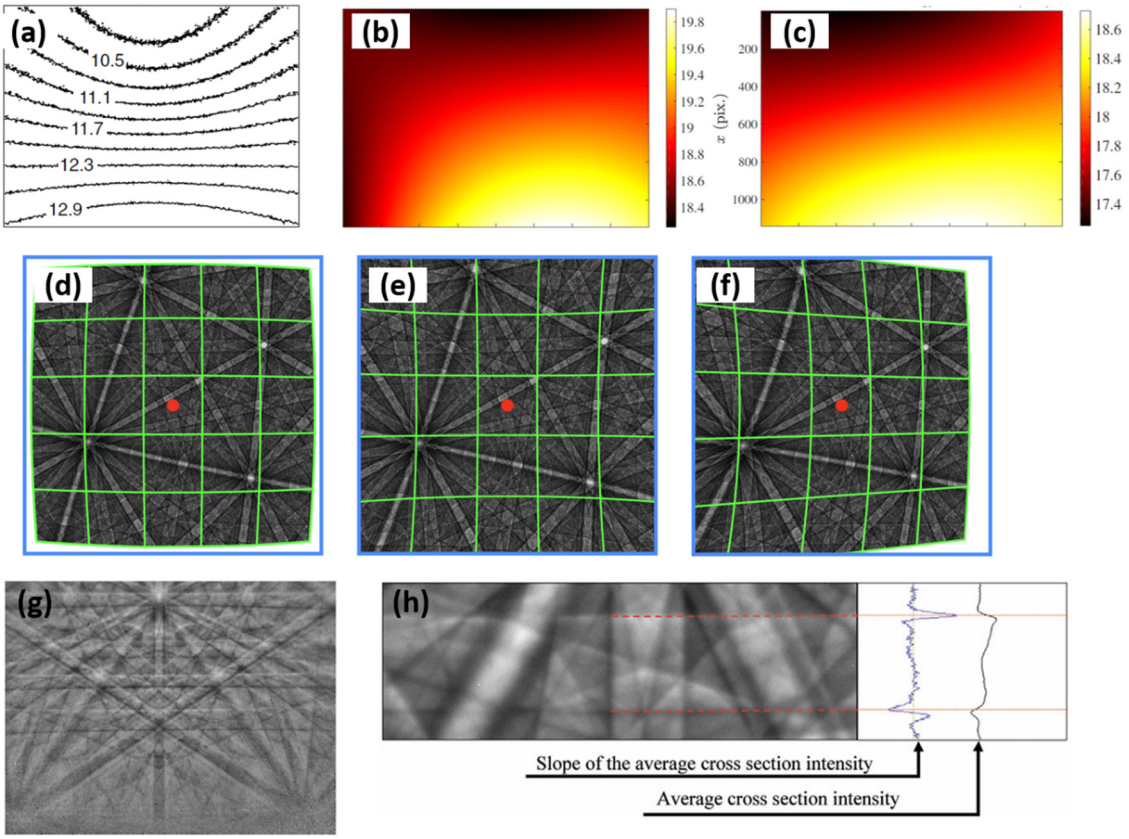

Figure 6. Examples of SEM-EBSD imperfections. a) Contour of average BSE energy distribution for a diffraction pattern with acceleration voltage of 15 kV [27]. b) Calibrated BSE energy distribution for an experimental EBSP. c) Simulated BSE energy distribution by Monte Carlo methods [22]. D to f) Illustrations of barrel, pincushion and tangential distortions of EBSPs respectively [23]. g) Experimental EBSD patterns from single crystal Si (111), 20 kV, with a tilt angle 56°. The K-bands of lower parts have reversed brightness [28]. h) The average cross-section brightness profile of a K-band. It is suggested to use the slope of the intensity profile to determine the band width [29].

9. LATTICE CONSTANTS

The lattice constant parameters were elusive for Hough-transform-based conventional EBSD algorithm, as it focusses on the angle between the K-bands rather than their width. Several groups have proposed different HR-EBSD techniques to access the lattice constants and hydrostatic dilations, mainly relying capturing the K-band width with sub-pixel precision. Saowadee *et al.* [29] proposes to set the maximum position of the slope of K-band brightness profile as the band edge, which was soon widely adopted by the community [25, 26, 30]. Lattice constant parameters are retrieved with a relative accuracy below 10^{-2} [30].

Information is inevitably lost in the transformation from (2D) full EBSP to (1D) brightness profile of K-bands, hence the full pattern match (FPM) between EBSP pairs would enhance the lattice parameter measurement precision. For example, Shi *et al.* [31] registers an experimental

pattern to several master patterns of different K-band widths, simulated with a constant lattice constant and varying energy levels of BSEs. High quality experimental patterns of an industrial Ni single crystal with TaC inclusions are tested. The in-plane absolute stress components and the lattice constant can be simultaneously obtained, as shown in the Ni results (Fig. 7). The Ni matrix at the tip of the TaC exhibits high tensile stresses. The lattice constant contrast of the cell interior (Ni_3Al) and the cell boundary (Ni) are highly visible and coincide with the secondary electron image. Both the systematic and random errors of the dilation results are reported to be below 10^{-3}.

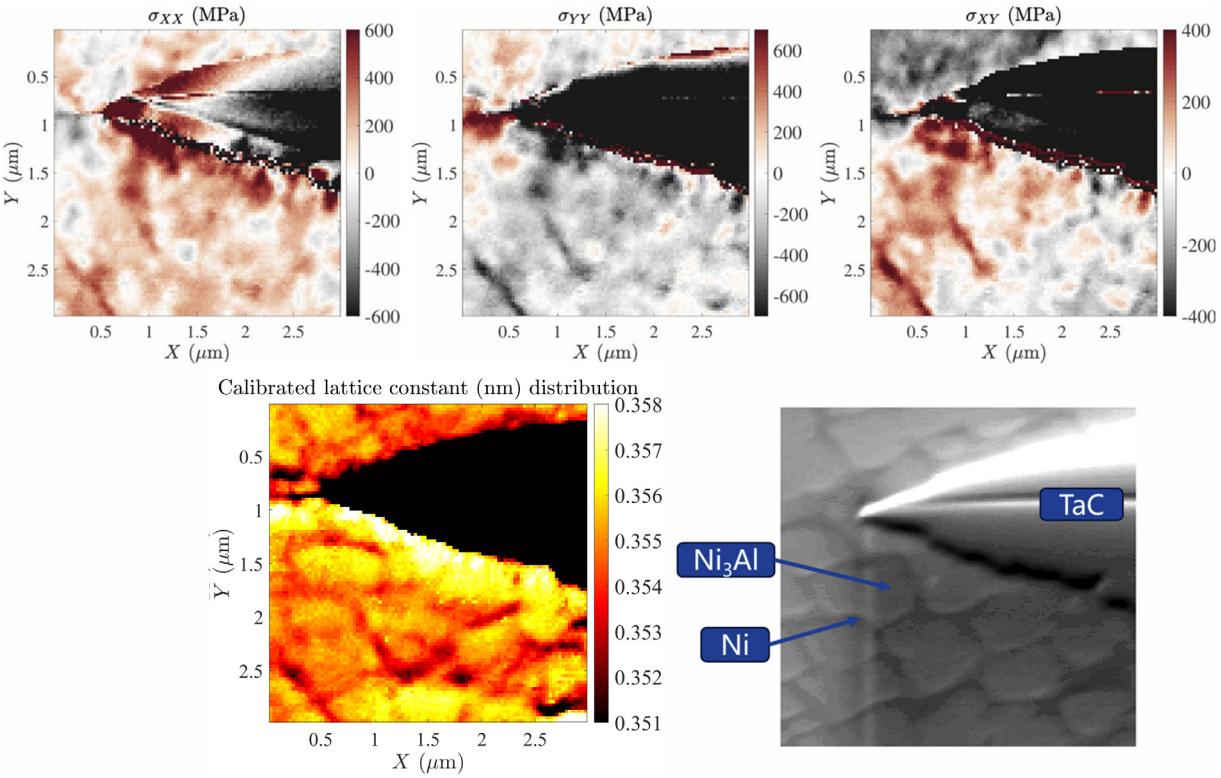

Figure 7. Characterisation of a Ni-Al/TaC [31]. Top: In-plane stress components $\sigma_{XX}, \sigma_{YY}, \sigma_{XY}$. Bottom) Distribution of the calibrated lattice constant of Ni-Al, and a secondary electron image of the sample, with the 3 phases indicated.

10. TEMPERATURE

Temperature is a key parameter that impacts samples, from the strength of metals to the reliability of microelectronic chips. There has been a lasting interest in the development of non-contact thermometry techniques. HR-EBSD is potentially a full-field, sub-micrometre resolution, non-destructive thermometer that requires no additional effort during routine data acquisition. Two major pathways were adopted in the community.

10.1. Thermal dilatation by evaluating the lattice constants

The thermal dilation of crystals results in the variation of K-band width, which can be identified by advanced EBSD analyses. Figure 8 shows a temperature measurement obtained via the thermal dilatation mechanism [32]. By calculating the cross-correlation coefficient of experimental patterns with master patterns simulated with different lattice constants, the width information of the Kikuchi band is precisely evaluated. Transformed into temperature using the coefficient of thermal expansion, the measurement uncertainty is evaluated to be 14 K for TKD patterns with a 24 ms exposure time [32].

10.2. The pattern blurriness

The atoms vibration around their equilibrium positions, quantified as the Debye-Waller factor, deviates the crystal from the perfect Bragg's condition and blurs the diffraction pattern. Figure 9a shows two EBSPs at 0 K and 300 K simulated by Bloch wave method. Patterns of lower temperature appear darker as the brightness is more concentrated at the central line of K-bands. The spatial frequency distribution of EBSPs can thus be used to evaluate the temperature with sub-micrometre spatial resolution. The temperature precision is estimated to be 13 K [33].

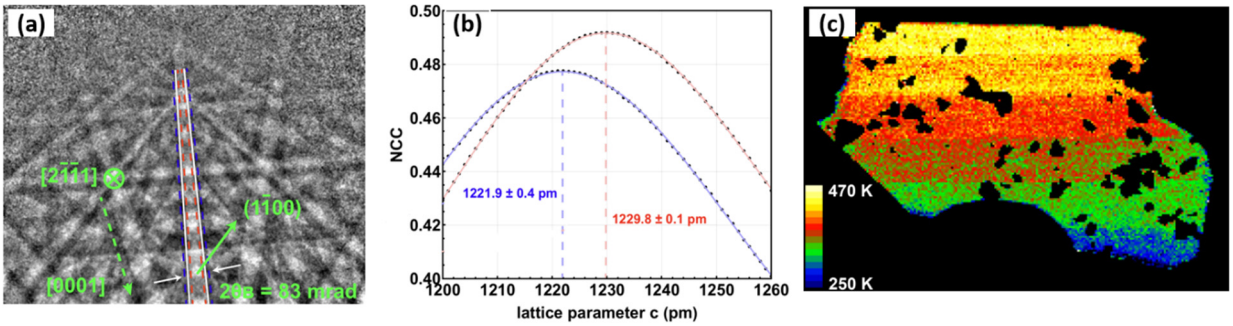

Figure 8. Temperature measurement by thermal dilation [32]. a) A TKD pattern from the middle of the MoS_2 flake. The band highlighted with solid white lines corresponds to the family of lattice plane 1$\bar{1}$11. The width of the Kikuchi bands varies with strain, with red and blue dashed lines indicating the directions of change that correspond to positive and negative strain respectively. b) Normalised cross-correlation coefficient (NCC) plot with master patterns calculated with different lattice constants for two different EBSPs. The position of the max NCC, or the best fit lattice parameter, is marked. c) Temperature map of the graphite flake while the heating power is varied six times during a TKD scan. The six different temperatures are visually distinguishable.

It should be noted that the uncertainty level of 14/13 K in the temperature measurement, obtained by exploiting the two above-mentioned phenomena is not yet deemed satisfactory for industrial applications. More precise data processing methods need to be developed, such as combining the above two effects or implementing more advanced FPM algorithms.

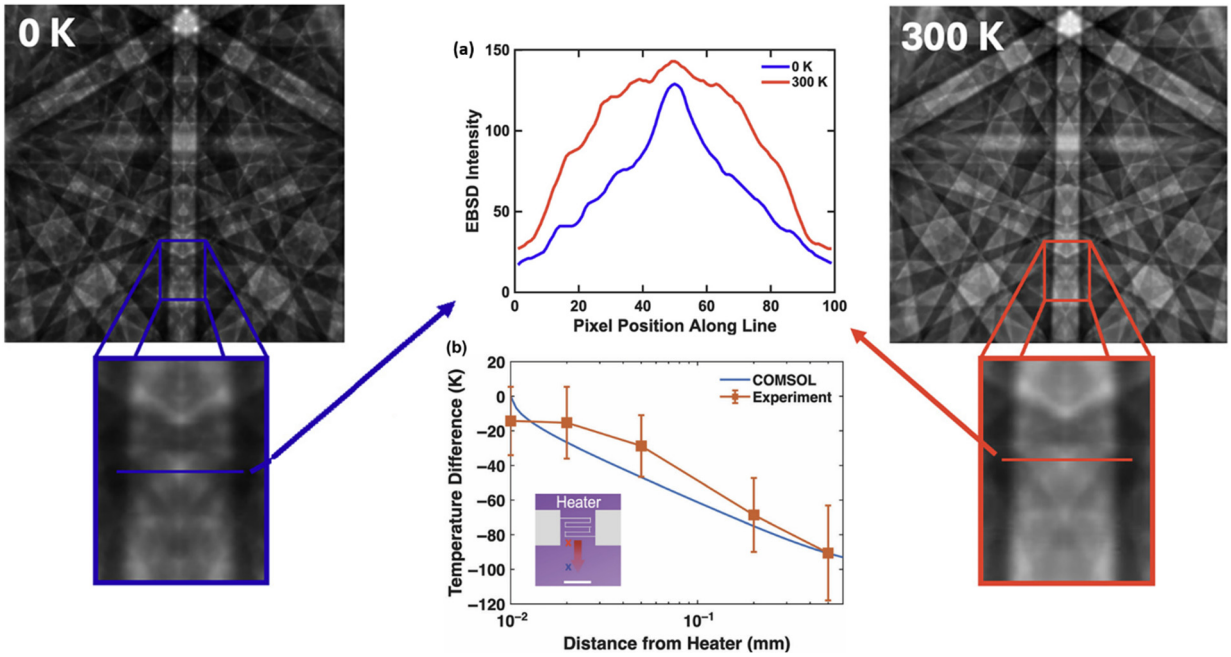

Figure 9. a) Illustration of the effects of temperature on EBSD patterns. The cross-section brightness profiles of the K-bands of higher temperature are more diffuse. b) The temperature evolution with distance from heater evaluated by EBSD and COMSOL simulation [33].

11. CONCLUSION

The interaction between the electron beam and the sample is complex and the data recorded by EBSD is large in volume. HR-EBSD techniques help to retrieve the rich information contained in the EBSPs. During the last two decades, numerous research groups have dedicated to advancing HR-EBSD experiments and algorithms. This talk summarises the continuingly growing list of physical quantities available by HR-EBSD, relative and absolute stress components, geometrically necessary and statistically stored dislocations, surface topography, lattice constant parameters, imperfections of EBSD system such as the pattern distortion, temperature … The increasing versatility and ever improving precision of HR-EBSD characterisation brings about new possibilities in materials science, micromechanics, and for the semiconductor industry.

12. ACKNOWLEDGEMENT

This work is financially supported by the National Natural Science Foundation of China [No. 52273229, 51901132] and the MAI (Materials Ageing Institute, http://themai.org).

13. REFERENCES

[1] Wilkinson A J, Meaden G and Dingley D J 2006 *Ultramicroscopy* **106** 307-313
[2] Maurice C, Driver J and Fortunier R 2012 *Ultramicroscopy* **113** 171-181
[3] Vaudin M D, Osborn W A, Friedman L H, Gorham J M, Vartanian V and Cook R F 2015 *Ultramicroscopy* **148** 94-104
[4] Plancher E, Petit J, Maurice C, Favier V, Saintoyant L, Loisnard D, Rupin N, Marijon J-B, Ulrich O, Bornert M, Micha J-S, Robach O and Castelnau O 2016 *Exp. Mechanics* **56** 483-492
[5] Ruggles T, Gilliland W, Fullwood D and Kacher J 2026 *Progr. Mater. Sci.* **157** 101585
[6] Britton T B, Maurice C, Fortunier R, Driver J H, Day A P, Meaden G, Dingley D J, Mingard K and Wilkinson A J 2010 *Ultramicroscopy* **110** 1443-1453
[7] Alkorta J, Marteleur M and Jacques P J 2017 *Ultramicroscopy* **182** 17-27
[8] Vermeij T, De Graef M and Hoefnagels J 2019 *Scripta Materialia* **162** 266-271
[9] Kurniawan C, Zhu C and De Graef M 2021 *Scripta Materialia* **190** 147-152
[10] Zhu C, Kurniawan C, Ochsendorf M, An D, Zaefferer S and De Graef M 2022 *Ultramicroscopy* **233** 113407
[11] Shi Q, Zhong H, Loisnard D, Nowell M, Mollens M, Chen Z, Wang H and Roux S 2024 *Mater. Characterization* **218** 114508
[12] Demir E, Kareer A, Hardie C and Tarleton E 2025 *Int. J. Plasticity* **195** 104464
[13] Pantleon W 2016 *Scripta Materialia* **58** 994-997
[14] Ruggles T J, Fullwood D T and Kysar J W 2016 *Int. J. Plasticity* **76** 231-243
[15] Zhong H, Shi Q, Dan C, You X, Zong S, Zhong S, Zhang Y, Wang H and Chen Z 2024 *Acta Materialia* **279** 120290
[16] Wang F, Stinville J C, Charpagne M, Echlin M, Agnew S R, Pollock T M, De Graef M and Gianola D S 2023 *Mater. Characterization* **197** 112673
[17] Wu K, Sun X, Liu B, Li Q, Wen W, Shi Q, Xu Z, Peng L, Wang H, Zhang Y and Forest S 2026 *J. Mechanics Phys. Solids* **212** 106597
[18] Callahan P, Echlin M, Pollock T and De Graef M 2017 *Microsc. Microanal.* **23** 730-740
[19] Singh S, Ram F and De Graef M 2017 *Microsc. Microanal.* **23** (Supplm. 1) 212-213
[20] Cheng L, Ming Y and Ding Z 2018 *New J. Phys.* **20** 113004
[21] Xiao X, Ma T, Shao L, Liu J, Shi Q, Cai C and Roux S 2026 *Micron* **204** 104025
[22] Shi Q, Jiao L, Loisnard D, Dan C, Chen Z, Wang H and Roux S 2022 *Mater. Characterization* **188** 111909
[23] Ernould C, Beausir B, Fundenberger J-J, Taupin V and Bouzy E 2021 *Ultramicroscopy* **221** 113158
[24] Shi Q, Plancher E, Loisnard D, Karamched P, Liu J, Chen Z, Wang H and Roux S 2022 *Mater. Characterization* **194** 112458
[25] Shi Q, Zhong H, Loisnard D, Wang L, Chen Z, Wang H and Roux S 2023 *Mater. Characterization* **202** 113022
[26] Wojciak K, Tokarski T, Cios G, Winkelmann A, Chulist R and Nolze G 2025 *Arch. Metall. Mater.* **70** 1619-1626
[27] Ram F and De Graef M 2018 *Phys. Rev. B, Cond. Matter* **97** 134104
[28] Winkelmann A and Nolze G 2010 *Ultramicroscopy* **110** 190-194

[29] Saowadee N, Agersted K and Bowen J 2017 *J. Microscopy* **266** 200-210
[30] Nolze G, Tokarski T, Rychlowski L, Cios G and Winkelmann A 2021 *J. Appl. Crystall.* **54** 1012-1022
[31] Shi Q, Loisnard D, Mollens M and Roux S 2025 *Microsc. Microanal.* **31** (Suppl. 1) 635-636
[32] Chen Y, Ling X, Lodico J, O'Neill T, Regan B and Mecklenburg M 2025 *Mapping temperature using transmission Kikuchi diffraction*. https://doi.org/10.48550/arXiv.2510.14175
[33] Gnabasik R, Nughays R O, Overholser A, Lin T, Kumar V, Adajian S, della Ventura N M, Gu M, Gianola D S and Liao B 2025 *Phys. Rev. Applied* **24** 064028